doi:10.1093/brain/awn016 *Brain* (2008), **131**, 1630–1645

Post-mortem correlates of *in vivo* PiB-PET amyloid imaging in a typical case of Alzheimer's disease

Milos D. Ikonomovic,[1,2] William E. Klunk,[2] Eric E. Abrahamson,[1] Chester A. Mathis,[3] Julie C. Price,[3] Nicholas D. Tsopelas,[2] Brian J. Lopresti,[3] Scott Ziolko,[3] Wenzhu Bi,[3] William R. Paljug,[1] Manik L. Debnath,[2] Caroline E. Hope,[1] Barbara A. Isanski,[1] Ronald L. Hamilton[4] and Steven T. DeKosky[1,2]

[1]Department of Neurology, [2]Department of Psychiatry, [3]Department of Radiology and [4]Department of Neuropathology, University of Pittsburgh School of Medicine, Pittsburgh, PA, 15213, USA

Correspondence to: Steven T. DeKosky, MD, Department of Neurology, 3471 Fifth Avenue, Suite 811, Pittsburgh, PA 15213, USA
E-mail: dekoskyst@upmc.edu

The positron emission tomography (PET) radiotracer Pittsburgh Compound-B (PiB) binds with high affinity to β-pleated sheet aggregates of the amyloid-β (Aβ) peptide *in vitro*. The *in vivo* retention of PiB in brains of people with Alzheimer's disease shows a regional distribution that is very similar to distribution of Aβ deposits observed post-mortem. However, the basis for regional variations in PiB binding *in vivo*, and the extent to which it binds to different types of Aβ-containing plaques and tau-containing neurofibrillary tangles (NFT), has not been thoroughly investigated. The present study examined 28 clinically diagnosed and autopsy-confirmed Alzheimer's disease subjects, including one Alzheimer's disease subject who had undergone PiB-PET imaging 10 months prior to death, to evaluate region- and substrate-specific binding of the highly fluorescent PiB derivative 6-CN-PiB. These data were then correlated with region-matched Aβ plaque load and peptide levels, [^{3}H]PiB binding *in vitro*, and *in vivo* PET retention levels. We found that in Alzheimer's disease brain tissue sections, the preponderance of 6-CN-PiB binding is in plaques immunoreactive to either Aβ42 or Aβ40, and to vascular Aβ deposits. 6-CN-PiB labelling was most robust in compact/cored plaques in the prefrontal and temporal cortices. While diffuse plaques, including those in caudate nucleus and presubiculum, were less prominently labelled, amorphous Aβ plaques in the cerebellum were not detectable with 6-CN-PiB. Only a small subset of NFT were 6-CN-PiB positive; these resembled extracellular 'ghost' NFT. In Alzheimer's disease brain tissue homogenates, there was a direct correlation between [^{3}H]PiB binding and insoluble Aβ peptide levels. In the Alzheimer's disease subject who underwent PiB-PET prior to death, *in vivo* PiB retention levels correlated directly with region-matched post-mortem measures of [^{3}H]PiB binding, insoluble Aβ peptide levels, 6-CN-PiB- and Aβ plaque load, but not with measures of NFT. These results demonstrate, in a typical Alzheimer's disease brain, that PiB binding is highly selective for insoluble (fibrillar) Aβ deposits, and not for neurofibrillary pathology. The strong direct correlation of *in vivo* PiB retention with region-matched quantitative analyses of Aβ plaques in the same subject supports the validity of PiB-PET imaging as a method for *in vivo* evaluation of Aβ plaque burden.

Keywords: Pittsburgh Compound-B; PiB; amyloid imaging; plaques; PET imaging

Abbreviations: Aβ = amyloid-β peptide; AC-PC = the plane of anterior comissure-posterior comissure; BA = Brodmann area; CAA = cerebral amyloid angiopathy; DVR = Logan distribution volume ratio; ELISA = enzyme linked immunoadsorbant assay; ERC = entorhinal cortex; FA = formic acid; IHC = immunohistochemistry; NFT = neurofibrillary tangles; PiB = Pittsburgh Compound-B; ROI = region-of-interest; Thio-S = thioflavin-S; VOI = volume-of-interest

Received October 28, 2007. Revised December 29, 2007. Accepted January 21, 2008. Advance Access publication March 12, 2008

Introduction

Clinically symptomatic Alzheimer's disease can be diagnosed with high accuracy at academic centres (Lopez *et al.*, 2000*a*, *b*), but diagnosis in the community is less accurate (Pearl, 1997). Non-Alzheimer's disease dementia cases are not infrequently misdiagnosed as Alzheimer's disease (Mayeux *et al.*, 1998), and an emerging issue is the accurate prediction of conversion of patients with mild

cognitive impairment (MCI) to Alzheimer's disease (Gauthier *et al.*, 2006). For optimal treatment, it is also critical to identify hallmark Alzheimer's disease pathology as early as possible. This pathology includes β-pleated sheet protein aggregates of amyloid-β (Aβ) peptides in senile plaques (SP) and hyperphosphorylated tau protein in neurofibrillary tangles (NFT) (Khachaturian, 1985; Mirra *et al.*, 1991; Consensus, 1998). The development of anti-amyloid therapies (Nicoll *et al.*, 2006) further emphasizes the need for a technology to assess treatment efficacy in individual patients. Thus sensitive *in vivo* markers of Alzheimer's disease brain lesions are needed (Consensus, 1998; Klunk, 1998; Growdon, 1999; Morris *et al.*, 2005; Thal *et al.*, 2006).

Positron emission tomography (PET) imaging of amyloid deposits (Klunk *et al.*, 2004; Verhoeff *et al.*, 2004; Small *et al.*, 2006) employs blood–brain barrier penetrant amyloid-binding compounds such as the thioflavin-T derivative Pittsburgh Compound-B (PiB) (Klunk *et al.*, 2001, 2004; Mathis *et al.*, 2002, 2004, 2005). Compared to age-matched, cognitively intact controls, Alzheimer's disease patients have 2- to 3-fold greater PiB retention on PET scans in brain areas known to have high amounts of fibrillar (i.e. Congo red and thioflavin-S labelled) Aβ plaques in Alzheimer's disease, such as frontal cortex and temporal lobe (Klunk *et al.*, 2004; Price *et al.*, 2005). Conversely, brain areas relatively unaffected by fibrillar Aβ pathology, such as the cerebellum, do not have increased PiB retention in Alzheimer's disease subjects. In agreement with these observations *in vivo*, studies of post-mortem Alzheimer's disease brain homogenates show that PiB binds preferentially to Aβ fibrils (Klunk *et al.*, 2003*a*), suggesting that PiB imaging could serve as a tool for monitoring changes in Aβ pathology in Alzheimer's disease. However, the evidence of a direct correlation between *in vivo* PiB-PET retention levels and Aβ plaques in the same subject is lacking. A recent study of a subject diagnosed with dementia with Lewy bodies, who at autopsy manifested severe vascular Aβ40 peptide-containing amyloid and infrequent SP, demonstrated that vascular amyloidosis can contribute significantly to PiB-PET signal (Bacskai *et al.*, 2007), as did a study of cerebral amyloid angiopathy (CAA) (Johnson *et al.*, 2007), while Lewy bodies themselves contributed little if at all to overall PiB-PET signal (Fodero-Tavoletti *et al.*, 2007). An *in vitro* study, comparing PiB autoradiography signal with Aβ/amyloid immuno/histology in adjacent autopsy tissue sections, reported a close correspondence of PiB signal with vascular amyloid and Aβ plaques in Alzheimer's disease, and with NFT in a non-Alzheimer's disease case (Lockhart *et al.*, 2007). However, the degree to which PiB binding to Aβ plaques compared to NFT contributes to *in vivo* recorded PiB retention signal, and the basis for region-specific differences in PiB retention levels in Alzheimer's disease brains *in vivo*, remains to be fully established.

In the present study we addressed these issues by examining the binding substrates of the highly fluorescent PiB derivative 6-CN-PiB in Alzheimer's disease post-mortem tissues collected from brain regions known to differentially accumulate neuritic and diffuse Aβ plaques and NFT, and to display differential PiB-PET retention levels *in vivo* (Klunk *et al.*, 2004). The physical, pharmacodynamic and pharmacokinetic properties of 6-CN-PiB are very similar to PiB (Mathis *et al.*, 2003), but the bright fluorescence of 6-CN-PiB greatly facilitates histochemical studies compared to the more weakly fluorescent parent compound, PiB. These combined histological/immunohistochemical analyses in brain tissue sections were supplemented by quantitative biochemical analyses of [^{3}H]PiB binding and Aβ peptide levels in brain tissue homogenates. We also examined the brain of an Alzheimer's disease subject who underwent PiB-PET imaging 10 months prior to death, to determine the relationship of ante-mortem PiB retention levels (determined by PET) to quantitative measures of 6-CN-PiB and Aβ labelled plaque load, neurofibrillary pathology, [^{3}H]PiB-binding levels and soluble and insoluble Aβ40 and Aβ42 peptide levels assessed post-mortem in the same brain regions of this subject. The results of these studies provide new insight into the basis for region-specific patterns of PiB binding *in vivo*, an understanding of which is critical for future evaluation of PiB-PET imaging during the course of Alzheimer's disease, and in the evaluation of effects of anti-amyloid therapies.

Methods

Clinical and neuropathological information: autopsy series

Brain tissues were obtained post-mortem from 27 dementia patients enrolled in the University of Pittsburgh Alzheimer's Disease Research Center (ADRC). Clinical diagnosis of Alzheimer's disease dementia utilized standard criteria (McKhann *et al.*, 1984). Mean Mini Mental Examination Score (MMSE) was 11 ± 8, mean age was 76 ± 11 years and mean duration of disease was 7 ± 4 years. Neuropathological diagnosis of 'definite Alzheimer's disease' was made by the established criteria (Mirra *et al.*, 1991; Consensus, 1998). Fifteen subjects had no other types of brain pathology besides occasional old infarcts; 11 had concomitant α-synuclein-immunoreactive neocortical Lewy bodies (Lewy body variant of Alzheimer's disease), and one subject had concomitant Parkinson's disease. Superior frontal and medial temporal cortices, parahippocampal gyrus, striatum and cerebellum were dissected at autopsy, immersed in cold 4% paraformaldehyde for 48 h, cryoprotected in sucrose and sectioned at 40 microns on a freezing sliding microtome. Tissue sections were collected serially in a cryoprotectant solution and stored at −20°C. Fresh-frozen tissue samples of frontal and occipital cortex grey matter were obtained from six of these Alzheimer's disease brains and were frozen at −80°C until analysis.

Clinical and neuropathological information: case study

A 64-year-old female with severe Alzheimer's disease (MMSE = 1 at the time of PiB-PET and MR imaging) was followed clinically in the University of Pittsburgh ADRC for 1 year. Dementia symptoms were first recorded 8 years prior to her death. Her apolipoprotein-E genotype was 3/4. The patient's mother, maternal aunt and uncle all had onset of Alzheimer's disease in their 80s. Her cognitive decline was described by family members as gradually progressive but more rapid in the 18 months prior to her death. At autopsy, the brain weighed 1070 g and upon gross examination was unremarkable except for cortical and hippocampal atrophy and minimal atherosclerosis of the circle of Willis. Multiple brain regions were sampled from the right hemisphere and flash frozen (unfixed) on dry ice for biochemical analyses; the left hemisphere was immersed in 10% formalin for histology.

PiB-PET and MRI scans and image analyses: case study

The subject underwent PiB-PET and MR imaging 10 months prior to death. Before the PET imaging session, a spoiled gradient recalled MR scan was obtained for anatomical region-of-interest (ROI) definition. MRI/PET image co-registration was performed using automated methods as previously described (Price *et al.*, 2005). PET scanning also was performed as previously described (Lopresti *et al.*, 2005); data were acquired using a Siemens/CTI ECAT HR+ scanner (3-dimensional mode, 63 image planes, 15.2 cm axial field of view) following the injection of ~555 MBq of high-specific activity (>21.4 GBq/μmol) PiB. PET emission data were acquired over 60 min (31 frames: 4 × 15 s, 8 × 30 s, 9 × 60 s, 2 × 180 s, 8 × 300 s), corrected for attenuation scatter, and radioactive decay, and reconstructed using filtered back-projection. The reconstructed image resolution was ~6-mm full width at half maximum in the transverse and axial planes. PiB retention levels were determined by the Logan distribution volume ratio (DVR), with the cerebellum as reference region, and were adjusted for partial volume effects (see below) (Lopresti *et al.*, 2005). Logan graphical analyses (Logan *et al.*, 1996) were performed for 35–60 min (5 points) intervals using input functions derived from cerebellar tissue radioactivity to yield the DVR as the outcome measure (Lammertsma and Hume, 1996). The DVR is a unitless value related directly to the free binding-site pool (B_{max}) and the ligand dissociation constant (K_d) (Mintun *et al.*, 1984), and is a measure of region-specific PiB retention (Lopresti *et al.*, 2005).

In vivo–in vitro correlation analyses: case study

From the left (formalin fixed) hemisphere, a 1-cm thick axial tissue slab was dissected by making a cut along the AC-PC plane (i.e. along a plane through the anterior and posterior commissures), and a second cut parallel and 1 cm dorsal to the AC-PC plane. This plane of section allowed for sampling from multiple cortical and subcortical regions known to be differentially affected with Aβ and NFT pathology, and also allowed for precise sampling of a matching clinical imaging plane. From this 1-cm thick axial tissue slab, 25 tissue cubes were chosen to sample the entire cortical ribbon and most of the subcortical nuclei present at this brain level (see Figs 4 and 5). All tissue cubes were ~1 × 1 cm except cube #25 (hippocampus: 0.5 × 0.5 cm) and cube #19 (occipital pole: polygon) that were adjusted to fit their respective anatomical boundaries in this axial plane of section. The 25 tissue cubes were dissected, cryoprotected (as described subsequently) and sectioned serially at 40 μm. Alternate sections were then divided into two sets. Selected tissue sections from one set were processed for histochemical staining with 6-CN-PiB, thioflavin-S (Thio-S) and X-34 compounds, and for immunohistochemistry (IHC) with anti-Aβ and anti-tau antibodies as described below (Fig. 4). All of the alternate tissue sections from each cube were combined and homogenized for the [^{3}H]PiB-binding assay (see below).

Co-registered MRI and PiB-PET images of the left hemisphere were oriented along the axial AC-PC plane. Guided by anatomical landmarks on the ventral surface (i.e. the AC-PC plane) of the tissue slab, the 25 ROIs were drawn in the AC-PC plane of the MRI. Except for the slight adjustments necessary due to post-mortem collapse of the ventricles, all ROIs on the MRI scan matched the tissue cubes taken from the autopsy tissue slab (Fig. 5). These ROIs were then copied onto three additional MRI planes superior to the AC-PC plane for a total of four adjacent 0.24-cm planes, to produce 25 volumes-of-interest (VOIs). The VOIs were all 1 × 1 × 1 cm except VOI #25 (caudal portion of the hippocampus; 0.5 × 0.5 × 1 cm) and the polygonal VOI #19 (occipital pole). To minimize inclusion of CSF space in the hippocampal VOI, ROI #25 was moved slightly from plane to plane. The entire set of 25 VOIs was then transferred from the MRI scan onto the co-registered PiB-PET scan (Fig. 5).

Histochemically assessed 6-CN-PiB plaque load was calculated as percent area, and biochemical [^{3}H]PiB binding and ELISA Aβ levels were calculated as picomoles per gram of tissue wet weight. Both of these post-mortem measures inherently corrected for (i.e. exclude) any partial volume effects by focusing only on tissue and excluding any contribution from CSF spaces. Therefore, the *in vivo* PiB-PET DVR values also were adjusted for partial volume effects by the use of a 2-component MRI-based partial-volume correction to adjust for the dilutional effect of expanded cerebrospinal fluid spaces (Meltzer *et al.*, 1999; Lopresti *et al.*, 2005). Because the placement of six of the VOI (i.e. 10–13, 15 and 24) resulted in <70% tissue in the VOI, and this could result in artefactually high corrected DVR values, only those VOI with >70% tissue ($n = 19$) were included in our analyses.

From the right hemisphere, fresh (unfixed) tissue samples were dissected from 14 regions: superior (BA9) and middle (BA46) frontal cortex, frontal pole (BA10), occipital cortex (BA18), superior (BA41), middle (BA22) and inferior (BA21) temporal cortex, inferior parietal cortex (BA40), cingulate gyrus (BA31), caudate nucleus, subiculum/entorhinal cortex, Ammon's horn, subcortical white matter and cerebellum. It should be noted that these frozen tissue samples from right hemisphere did not correspond exactly to the 25 tissue cubes dissected from the formalin-fixed (left hemisphere) slab at the AC-PC level, but were contained within the standard VOI set routinely sampled in our *in vivo* PiB-PET studies (Price *et al.*, 2005). Frozen tissue samples were homogenized (150 mg/ml) in a tissue homogenization buffer [250 mM sucrose, 20 mM Tris base and protease inhibitors (Sigma #8340 protease inhibitor cocktail; 10 μl per millilitre buffer)] using a glass vessel and piston-type Teflon pestle. An aliquot of the 150 mg/ml homogenate was used for the Aβ ELISA; another aliquot was diluted to 10 mg tissue/ml with phosphate-buffered saline (PBS, pH 7.4) for the [^{3}H]PiB-binding assay (see below). For correlation analyses of these post-mortem biochemical assays and *in vivo* PiB-PET retention levels, these 14 areas were mapped

Table 1 Summary of histofluorescent markers and antisera used for histological and immunohistochemical analyses

Histofluorescent cmpd	Affinity	Concentration	Source (Reference)
6-CN-PiB	β-pleated sheet	10 μM	Dr W.E. Klunk (Mathis *et al.*, 2003)
Thioflavin S	β-pleated sheet	0.05%	Sigma (Guntern *et al.*, 1992)
X-34	β-pleated sheet	100 μM	Dr W.E. Klunk (Ikonomovic *et al.*, 2006)
Antisera (Host)	**Epitope**	**Dilution**	
b6E10 (mouse)	Aβ aa3–10	1:3000	Signet (Kim *et al.*, 1990)
AT8 (mouse)	Ser-202 (P) of tau	1:10,000	Signet (Mercken *et al.*, 1992)
Aβ40 (rabbit)	Ala-40; $Aβ_{1-40}$	1:1000	Chemicon (Kamal *et al.*, 2001)
Aβ42 (rabbit)	Ala-42; $Aβ_{1-42}$	1:1000	Chemicon (Kamal *et al.*, 2001)
K9JA (rabbit)	Repeat domain of tau	1:10,000	Dako (Thies *et al.*, 2007)
10D5 (mouse)	Aβ aa3–6	1:3000	Elan (Hyman *et al.*, 1992)

b = biotinylated.

onto corresponding VOIs drawn on the MR image (performed on the same day as the PiB-PET study) of the same hemisphere. VOIs were then transferred to the corresponding PiB-PET image for calculation of the DVR values (as described earlier), and the values correlated with the results of Aβ ELISA and [^{3}H]PiB-binding analyses (as below).

6-CN-PiB, X-34 and Thio-S histofluorescence

Tissue sections were slide mounted and processed for attenuation of lipofuscin autofluorescence (Guntern *et al.*, 1992). 6-CN-PiB was used at concentrations of 100 nM, 1 μM, 10 μM and 100 μM. The 10-μM concentration (Table 1) provided the optimal signal to noise ratio, and was used for the regional and double labelling analyses in both the autopsy series tissues and in sections from the 25 tissue cubes from the PiB-PET case. Sections were incubated in 6-CN-PiB for 45 minutes, dipped three times in phosphate buffer (PB; 0.1 M), followed by a 1-min differentiation in a solution containing 132.9 mM NaCl, 8.7 mM K_2HPO_4 and 1.5 mM KH_2PO_4 (pH 7.4), and coverslipped with Fluoromount (Electron Microscopy Services, Hatfield, PA). Tissue sections were also processed for Thio-S or X-34, a fluorescent derivative of Congo red, as previously described [Table 1; (Ikonomovic *et al.*, 2006)].

Immunohistochemistry

IHC was performed on free-floating tissue sections as previously described (Ikonomovic *et al.*, 2006). The 4% paraformaldehyde fixed tissue sections from ADRC Alzheimer's disease autopsy series were washed in PB, incubated in 70% formic acid (FA) and washed in PB. Endogenous peroxidase activity was inhibited by 0.3% H_2O_2 in 0.1 M Tris-buffered saline containing 0.25% Triton X-100 (TBST) for 45 min. Sections were then rinsed in TBST and incubated in 3% normal serum in TBST for 30 min followed by two 10-min rinses in 1% normal serum in TBST. Sections were then incubated overnight at 4°C in polyclonal $Aβ_{x-40}$ and $Aβ_{x-42}$ antisera, or the monoclonal 6E10 ($Aβ_{1-16}$) antibody (Table 1). Additional primary antibodies included anti-Aβ 10D5, pan-tau and phospho-tau AT8 (Table 1), used as described earlier except for omission of the FA incubation step. After washing in 1% normal serum in TBST, sections were incubated for 1 h in the species-appropriate biotinylated IgG (Vector Laboratories, Burlingame, CA; in 1% normal serum in TBST), except for the biotinylated 6E10. The sections were washed in TBST and processed with the avidin-biotin Elite kit (Vector Labs) in TBST for 1 h at room temperature. After washing repeatedly in imidazole acetate buffer (IAB), they were exposed to a solution containing 0.05% 3′,3-diaminobenzidine tetra-hydrochloride (DAB)/0.0015% H_2O_2 for 4 min, washed in IAB, mounted on gelatinized slides, dehydrated in alcohols, cleared in xylene and coverslipped with Permount (Fischer). The PiB-PET autopsy case sections were processed identically, with b6E10 and AT8 (Table 1) IHC performed following a 30-min incubation in 95% FA.

Dual IHC and histochemistry

To detect neuritic plaques, 6-CN-PiB labelled tissue sections were imaged, photobleached and then counterstained with either X-34 or Thio-S, to determine the extent of 6-CN-PiB labelling of neuritic plaques (containing X-34 or Thio-S labelled dystrophic neurites) and neurofibrillary tangles (labelled with either X-34 or Thio-S). The validity of this procedure was confirmed in an additional set of tissue sections that were either double immunolabelled with a monoclonal antibody to detect Aβ (10D5) and a polyclonal antiserum to detect tau (Table 1), or single-labelled with tau, and then counterstained with 6-CN-PiB. Tau IHC was performed as above, except that alkaline phosphatase-conjugated secondary antibodies and the Vector Blue substrate were used, and sections were pre-treated with levamisole (Vector) to prevent endogenous phosphatase activity. This procedure distinguished neuritic (10D5-immunoreactive plaques with tau-immunoreactive dystrophic neurites) and non-neuritic (10D5-immunoreactive plaques lacking tau- immunoreactive neurites) plaques. 6-CN-PiB counterstaining of IHC-processed sections followed removal of the chromogen using the tissue autofluorescence quenching procedure (Guntern *et al.*, 1992).

In vitro [^{3}H]PiB-binding assay

Formalin-fixed tissue samples were homogenized with a Polytron tissue homogenizer (PT 10/35, Brinkman Instruments Inc., Westbury, NY) at room temperature for 30 s at setting 6 in PBS (137 mM NaCl, 3 mM KCl, 10 mM sodium phosphate; pH 7.0) at a concentration of 10 mg brain/ml. Fresh-frozen tissue homogenates were diluted from 150 mg/ml in tissue homogenization buffer (see above) to 10 mg/ml with PBS and then re-homogenized with the PT 10/35 as described earlier. The homogenates were aliquoted and frozen at −80°C until used (within 2 months)

for binding assays. No significant changes in binding characteristics were observed in samples assayed repeatedly over this time period. Unlabelled PiB was dissolved in DMSO at 400 μM (to yield <1% DMSO in the final assay). This stock solution was diluted with PBS to achieve the desired concentration in the final assay. For determination of [^{3}H]PiB binding in homogenates of Alzheimer's disease brains, 1 nM [^{3}H]PiB (American Radiolabeled Chemicals, St. Louis, MO; specific activity 72.4 Ci/mmol) was incubated with 100 μg tissue in 1 ml PBS. Non-specific binding was defined as the number of counts remaining in the presence of 1 μM unlabelled PiB. The binding mixtures were filtered through a Whatman GF/B glass filter using a Brandel M-24R cell harvester (Gaithersburg, MD) and rapidly washed five times with 3 ml PBS. The filters were counted in Cytoscint-ES after thorough vortexing and resting overnight. Results were corrected for non-specific, non-displaceable binding in the presence of 1 μM PiB and expressed as picomoles [^{3}H]PiB bound per gram of wet tissue weight in the homogenate. Linearity of [^{3}H]PiB binding was confirmed using 1 nM [^{3}H]PiB and 20–500 μg/ml of the Alzheimer's disease brain homogenate with the highest level of [^{3}H]PiB binding. Linearity with respect to [^{3}H]PiB was confirmed using 100 μg tissue/ml and 1 to 6 nM [^{3}H]PiB. The amount of [^{3}H]PiB bound by this method has been shown to correlate highly with the total number of PiB-binding sites (i.e. the B_{max}; $r = 0.99$) (Klunk *et al.*, 2005) and, importantly, mimics the low nanomolar concentrations of radioactive PiB achieved in human brain during a PET study.

For synthetic Aβ fibril-binding studies, $Aβ_{1–40}$ or $Aβ_{1–42}$ (Bachem Biosciences, King of Prussia, PA) were aggregated as previously described (Klunk *et al.*, 2001). Binding studies were performed with slight modifications of a procedure previously described in detail (Klunk *et al.*, 2003*a*). The K_d and B_{max} values for [^{3}H]PiB binding to Aβ fibrils were determined using increasing concentrations of [^{3}H]PiB between 0.2 and 1 nM and, to achieve total PiB concentrations from 1 to 1000 nM, a constant 1-nM concentration of [^{3}H]PiB plus additional unlabelled PiB. The labelled and unlabelled PiB were prepared in 950 μl PBS. Binding was initiated by addition of 50 μl of a 4 μM suspension of Aβ fibrils in PBS (in triplicate) and the samples were incubated at 22°C for 60 min. Filtration was performed as described earlier for brain homogenates except that the filters were washed only three times with 3 ml PBS before counting.

Aβ enzyme linked immunoadsorbant assay (ELISA)

$Aβ_{1–40}$ and $Aβ_{1–42}$ peptides were quantified in both soluble (diethylamine, DEA) and insoluble (FA extracted) Aβ fractions following a published protocol (DeKosky *et al.*, 2007). The soluble fraction was prepared by homogenizing the tissue in 0.4% DEA in 100 mM NaCl, centrifuging at 135 000 *g* at 4°C for 1 h and neutralizing the supernatant with 0.5 M Tris–Cl. The insoluble fraction was prepared by homogenizing the pellet in 70% FA for 1 min, then centrifuging at 109 000 *g* at 4°C for 1 h. The supernatant was then neutralized with 1 M Tris, 0.5 M sodium phosphate. Both soluble and insoluble fractions were assayed using a fluorescent-based ELISA (Biosource; Camarillo, CA) with a capture antibody specific for the NH_2-terminus of Aβ (amino acids 1–16), and detection antibodies specific for Aβ peptides Aβ40 and Aβ42. Values were determined from standard curves using synthetic $Aβ_{1–40}$ and $Aβ_{1–42}$ peptides (Biosource) and were expressed as picomoles per milligram wet brain tissue. 'Total' Aβ levels refer to the sum of $Aβ_{1–40}$ and $Aβ_{1–42}$ values.

Plaque load analysis

Plaque load was determined by calculating the percent area labelled either immunohistochemically ($Aβ_{x–40}$, $Aβ_{x–42}$, 6E10) or histofluorescently (6-CN-PiB) in tissue sections. For the ADRC autopsy series brain tissue, nine randomly chosen areas were imaged on three sections for each brain region examined from each case. For correlation of *in vivo* PiB (PET) DVR levels with region-matched post-mortem quantitation of 6-CN-PiB histofluorescence and Aβ and phosphotau IHC, a 1000 by 750 μm field of the greatest plaque or NFT frequency was imaged in two sections chosen randomly from each of the 25 tissue cubes; plaque load was determined from the percent area occupied by Aβ-immunoreactive or 6-CN-PiB positive plaques, while the AT8 (phosphotau) immunoreactive 'load' represented percent area occupied by all AT8-immunoreactive structures (including NFTs, neuropil threads and other neuritic elements) in the field. An independent check of the representative nature of the two sections chosen randomly for each histological analysis was made by determining the total Aβ plaque load by 6E10 IHC in three additional sections chosen randomly from each of the 25 tissue cubes; these data correlated strongly with the original dataset. Microscope settings were held constant throughout the sampling. Images were then converted to binary using the public domain NIH Image program (available at: http://rsb.info.nih.gov/nih-image/). A predetermined threshold value was held constant throughout the analysis. Percent area values were obtained by dividing area labelled by total area sampled.

Statistical analysis

Correlation analyses were performed using Spearman rank order correlation. Statistical significance was set at 0.05 (two-sided).

Results

Characterization of 6-CN-PiB histofluorescence in Alzheimer's disease brain tissue from autopsy cases

6-CN-PiB binds primarily to Aβ plaques in Alzheimer's disease cortex

At concentrations of 1–10 μM, 6-CN-PiB fluorescent signal was detected almost exclusively in amyloid plaques and (when present) large, amyloid-laden blood vessels (Fig. 1A). The morphology of 6-CN-PiB labelled plaques was diverse, both within and between brain regions examined (see Table 2 for region-specific plaque terminology). In the neocortex, entorhinal cortex (ERC) and hippocampus, 6-CN-PiB robustly labelled compact/cored plaques, while diffuse/amorphous plaques were less prominently labelled (Fig. 1). No differences in the type of 6-CN-PiB labelled structures were observed at higher concentrations (e.g. 100 μM). At 100 nM, the lowest concentration tested, the overall intensity of 6-CN-PiB fluorescence was considerably reduced, and diffuse/amorphous plaques in the cortical and hippocampal regions were difficult to discern while

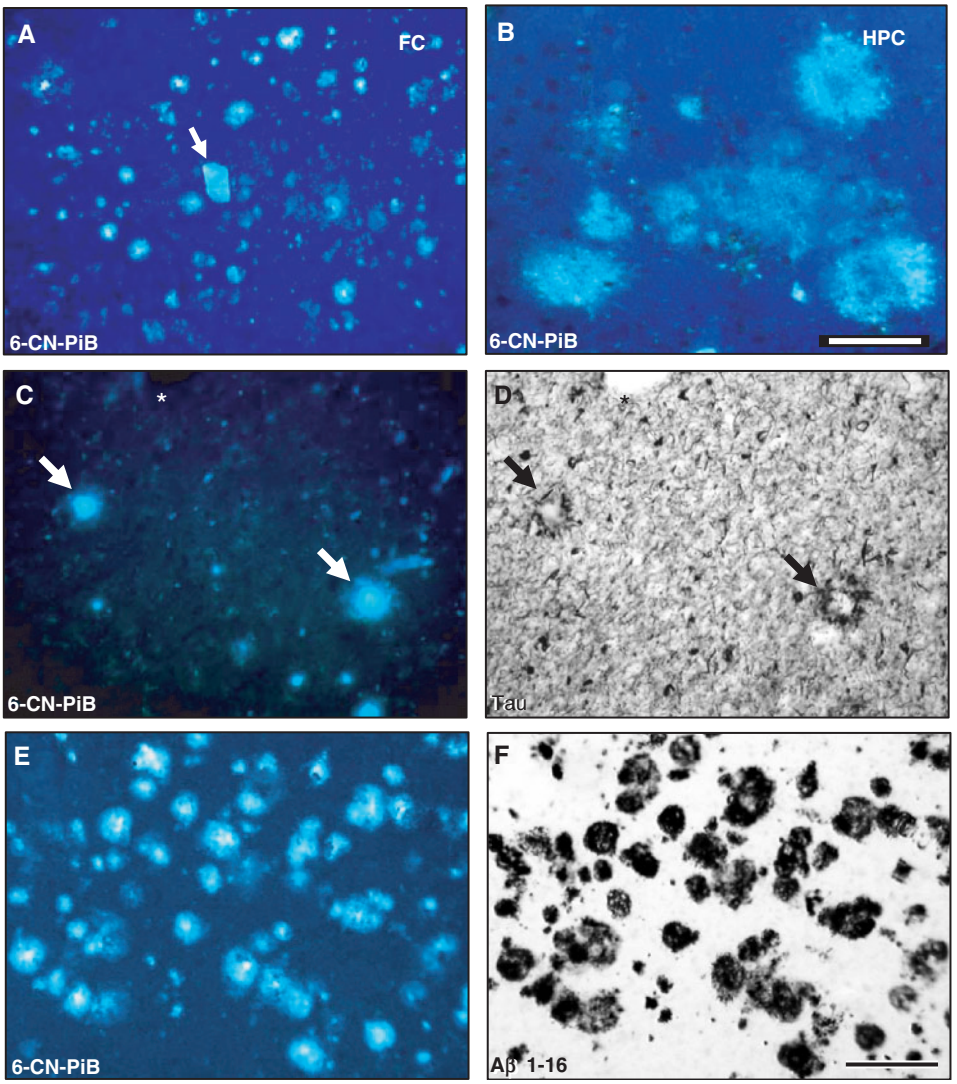

Fig. 1 Regional variations in 6-CN-PiB fluorescence signal in Alzheimer's disease brain tissue. In the frontal cortex (FC), 6-CN-PiB histofluorescence is seen in numerous compact/cored and diffuse plaques, and in an isolated large blood vessel with amyloid angiopathy (**A**, arrow). Amorphous diffuse plaques in the hippocampus (HPC; **B**) are 6-CN-PiB positive, but have lower fluorescence intensity compared to cored/compact 6-CN-PiB labelled plaques. 6-CN-PiB histofluorescence is prominent in cores of neuritic plaques identified by the presence of tau-immunoreactive dystrophic neurites (**C** and **D**; double labelling of the same Alzheimer's disease frontal cortex tissue section with tau IHC; asterisk denotes a tissue landmark, matched plaques are marked by arrows). 6-CN-PiB and Aβ immunoreactivity co-localize in plaques in an Alzheimer's disease frontal cortex (**E**, **F**; tissue section double labelled for 6-CN-PiB histofluorescence and Aβ immuhistochemistry with 10D5 antibody). Both markers are seen exclusively in amyloid plaques. Scale bar = 175 μm (**A**), 100 μm (**B–F**).

compact/cored plaques and vascular deposits were still detectable. 6-CN-PiB was not detectable in dystrophic neurites and neuropil threads (see below). Double-labelling experiments, combining 6-CN-PiB with tau IHC to reveal the presence or absence of dystrophic neurites in plaques, demonstrated that 6-CN-PiB labelled plaques both with (neuritic) and without (non-neuritic) tau-positive dystrophic neurites (Fig. 1).

No 6-CN-PiB labelling was detected in brain areas that were free of Aβ plaques as determined by Aβ IHC. There was an apparent one-to-one co-localization between 6-CN-PiB fluorescent plaques and Aβ immunoreactive plaques in cortical regions (Fig. 1), resulting in a direct correlation between plaque loads determined using these two markers ($r = 0.56$, $P = 0.009$). 6-CN-PiB labelled both Aβ42- and Aβ40-immunoreactive plaques (Supplementary Fig, 1A–D). Compact/cored Aβ40- and Aβ42-immunoreactive plaques were most intensely labelled, while diffuse/amorphous Aβ42 deposits were more lightly labelled. Plaque load analysis (by percent area; see Supplementary Fig. 1E) demonstrated a direct correlation between cortical plaque loads determined with 6-CN-PiB and with antibodies to either Aβ42 ($r = 0.82$, $P = 0.0002$) or Aβ40 ($r = 0.58$, $P = 0.011$).

6-CN-PiB labelling was not detectable in plaque-containing Alzheimer's disease tissue sections pre-treated

Table 2 6-CN-PiB (10 μM) labeling intensity in different plaque types and amyloid-containing structures in 4% paraformaldehyde fixed, 40 μM thick tissue sections

Plaque type	6-CN-PiB intensity	X-34 intensity
Compact/cored (NC, PhG, Crbl)		
Neuritic	++++	++++
Non-neuritic	++++	++++
Diffuse		
Amorphous (NC, PhG)	++	++
Cloud-like (Str)	++	++
Fleecy (Crbl)	0	++
Non-plaque amyloid	**6-CN-PiB intensity**	**X-34 intensity**
Vascular	++++	++++
Neurofibrillary tangles iNFT	+[a]	++++
Neurofibrillary tangles eNFT	+++	++++
Neuropil threads	0	++++
Dystrophic neurites	0	++++

0 = no 6-CN-PiB fluorescence signal; + = very light fluorescence barely above backgrounds; ++ = light fluorescence; +++ = moderate fluorescence; ++++ = intense fluorescence. NC = neocortex; PhG = parahippocampal gyrus; Str = striatum; Crbl = cerebellum; iNFT = intracellular NFT; eNFT = extracellular NFT.

[a]Only a small proportion of tangles per section detected in entorhinal cortex and subiculum.

with formic acid, which disrupts β-pleated sheets (Kitamoto *et al.*, 1987), and conversely, treating 6-CN-PiB processed tissue with formic acid abolished 6-CN-PiB labelling. The pattern of 6-CN-PiB plaque labelling matched that observed using two other amyloidal-binding compounds, Thio-S and X-34 (see Fig. 3); the latter two compounds' labelling of plaques was comparable, except that X-34 was more sensitive in detecting diffuse plaques.

6-CN-PiB is not detectable in cerebellar diffuse plaques

Similar to the pattern of 6-CN-PiB labelling of diffuse plaques in cortical and hippocampal regions, 6-CN-PiB labelling was detected in diffuse cloud-like plaques in the striatum (Fig. 2A); these plaques matched the pattern of Aβ-immunoreactive and X-34 histofluorescent diffuse plaques in this region (data not shown). In the cerebellum, however, 6-CN-PiB fluorescence was not detectable in diffuse plaques, although in adjacent tissue sections there were abundant diffuse Aβ-immunoreactive and X-34-positive plaques in the cerebellar cortical molecular layer (Fig. 2B–D). The only types of cerebellar structures detectable with 6-CN-PiB were large blood vessels (when present) and small to medium size compact plaques in the Purkinje cell layer. These structures also showed X-34 fluorescence signal (Fig. 2D inset).

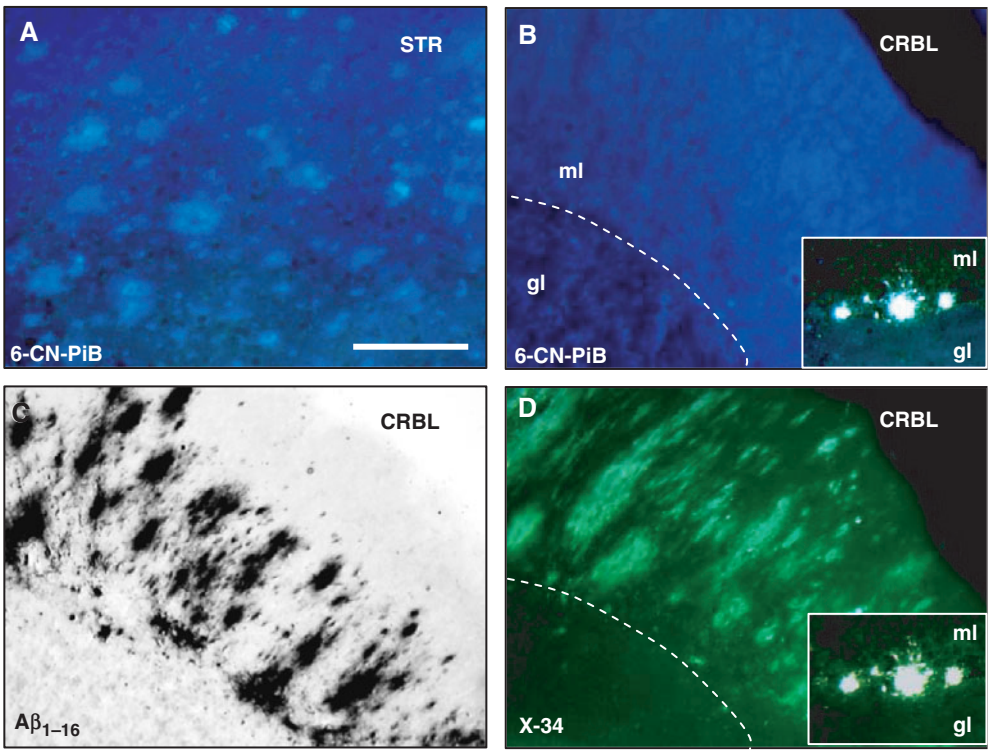

Fig. 2 6-CN-PiB histofluorescence is detectable in cloud-like diffuse plaques in the caudate nucleus of the striatum (STR; **A**). In the cerebellum (CRBL), 6-CN-PiB labelling is not appreciably above background levels (**B**), although the adjacent tissue sections processed for Aβ IHC (**C**, 10D5 antibody) and X-34 (**D**) show fleecy diffuse plaques in the molecular layer (ml) of cerebellar cortex (dotted line in **B** and **D** approximates the Purkinje cell layer). In the Purkinje cell layer, some isolated small compact plaques are detectable with both 6-CN-PiB and X-34 (inserts in **B** and **D**; gl, granular layer). Scale bar = 150 μm (**A–D**), 75 μm (Inset).

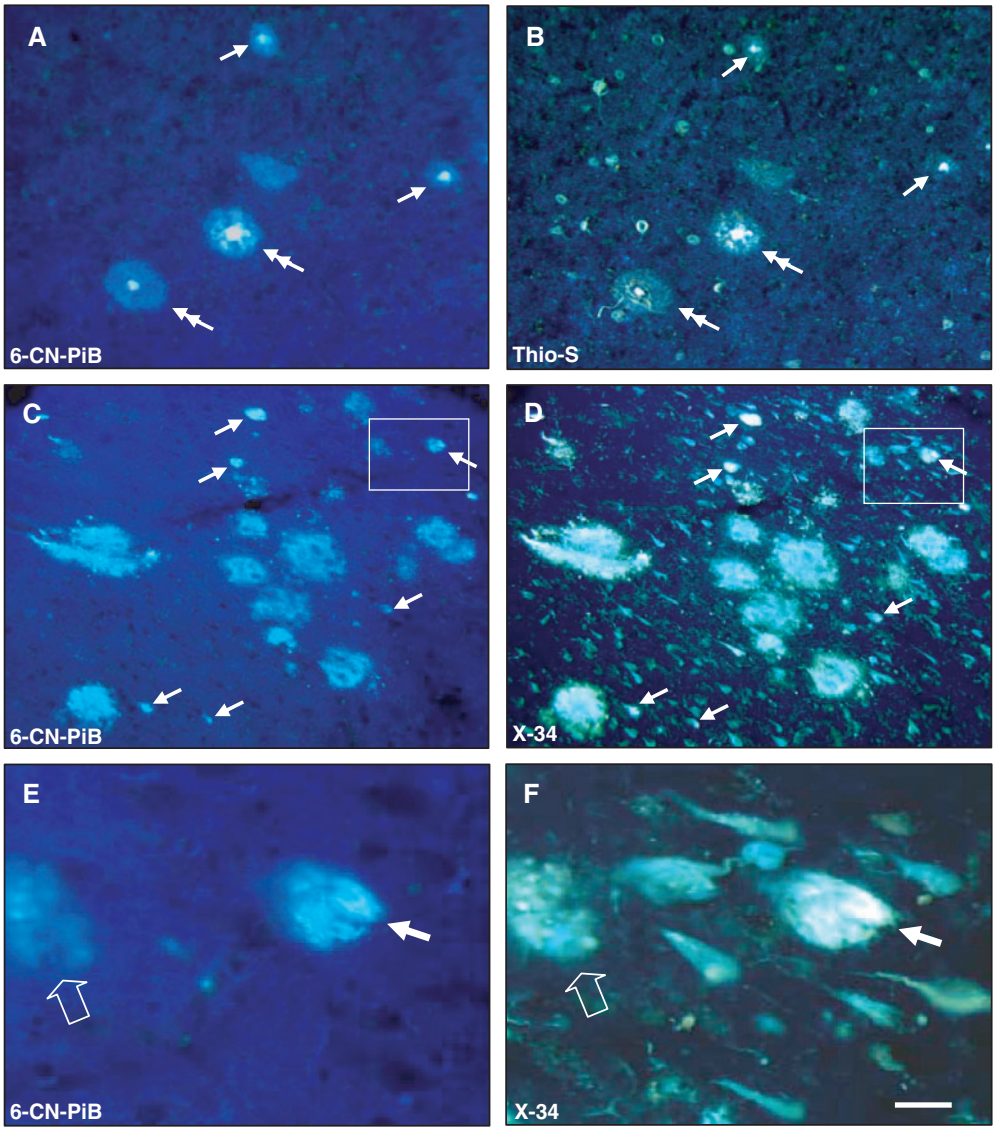

Fig. 3 Co-localization of 6-CN-PiB (**A, C, E**) with Thio-S (**B**) and X-34 (**D, F**) in plaques, but not in NFT in Alzheimer's disease temporal cortex (**A, B**), and hippocampus (**C–F**). Large cored plaques (double arrows) and small burnt out plaques (arrows) are labelled with both 6-CN-PiB and Thio-S in the temporal cortex, but Thio-S also labels numerous NFT that are not detectable with 6-CN-PiB (**A, B**). There is a good co-localization of 6-CN-PiB and X-34 in plaques in the hippocampus (**C, D**). X-34 also labels an array of neurofibrillary pathology in the hippocampus (**D**); only small numbers of these structures are detectable with 6-CN-PiB (**C**, arrows). **E** and **F** represent boxed areas in **C** and **D**, respectively, and illustrate a structure labelled with both 6-CN-PiB and X-34 (small arrow) that resembles an extracellular NFT with distinct bundles of longitudinally oriented fibrils that are loosely dispersed in the neuropil. A small diffuse plaque is also double labelled (empty arrow), while the rest of the X-34 positive NFT in the field are not detectable with 6-CN-PiB. Scale bar = 75 μm (**A–D**), 25 μm (**E, F**).

6-CN-PiB binding is absent from dystrophic neurites, neuropil threads and the majority of neurofibrillary tangles

6-CN-PiB was not detected in neocortical NFT, or in the vast majority of NFTs in the ERC and subiculum/CA1 that were detectable with tau IHC and Thio-S or X-34 histology in the same tissue sections (Fig. 3). In the ERC and subiculum/CA1, occasional 6-CN-PiB labelled NFT had a distinct morphology of extracellular 'tombstone' tangles (eNFT), enlarged NFT-like structures consisting of longitudinally oriented bundles of fibrils (Fig. 3C–F). In the ERC layer II cell islands, there were abundant NFT intensely labelled by X-34, while 6-CN-PiB labelling of these NFT was sparse. The same pattern of almost exclusive labelling of plaques in the ERC was also observed with BTA-1 (PiB) histochemistry (see Supplementary Fig. 2). In the hippocampus of one subject with large numbers of tau-immunoreactive and X-34 labelled intracellular NFT, but no Aβ plaques, there was no detectable 6-CN-PiB labelling (see Supplementary Fig. 3). 6-CN-PiB did not label neuritic elements such as tau-immunoreactive

dystrophic neurites and neuropil threads, all of which were detectable with X-34.

Direct correlation between quantitative [^{3}H]PiB binding and Aβ peptide (ELISA) levels in homogenates of Alzheimer's disease brain tissue from autopsy cases

In agreement with the 6-CN-PiB labelling of both Aβ40 and Aβ42 immunoreactive plaques in Alzheimer's disease brain tissue as described earlier, [^{3}H]PiB bound equally well to synthetic Aβ fibrils formed *in vitro* from either $A\beta_{1–40}$ or $A\beta_{1–42}$ peptides. The high-affinity K_d for [^{3}H]PiB binding was 0.90 nM for $A\beta_{1–40}$ and 0.95 nM for $A\beta_{1–42}$ (Supplementary Fig. 4A). The B_{max} values of the high-affinity sites were 0.42 pmol [^{3}H]PiB/nmol $A\beta_{1–40}$ and 0.46 pmol [^{3}H]PiB/nmol $A\beta_{1–42}$. This stoichiometry was similar to that previously reported (Klunk *et al.*, 2005). The low-affinity components had K_d values of 70–145 nM and thus represent binding that would not be relevant *in vivo* where [^{11}C]PiB concentrations are on the order of 1 nM or less (Klunk *et al.*, 2005). Using 1 nM [^{3}H]PiB, there was a direct correlation between *in vitro* [^{3}H]PiB binding and total (i.e. combined $A\beta_{1–40}$ and $A\beta_{1–42}$) insoluble Aβ in post-mortem frozen tissue homogenates of frontal and occipital cortices from six Alzheimer's disease subjects ($r = 0.95$, $P < 0.0001$, Supplementary Fig. 4B). There was no significant correlation of [^{3}H]PiB binding with soluble Aβ peptides.

Direct correlation of *in vivo* PiB-PET retention levels with region-matched post-mortem quantitations of PiB binding, plaque load and Aβ peptide levels

Regional correlations of ante-mortem PiB retention (DVR) levels and post-mortem analyses of PiB binding and Alzheimer's disease pathology in the same individual were possible because one Alzheimer's disease subject underwent *in vivo* PiB-PET, and a brain autopsy was performed 10 months later. In this case, the final neuropathological diagnosis by CERAD criteria (Mirra *et al.*, 1991) was 'definite Alzheimer's disease', and the Braak stage (Braak and Braak, 1991*b*) was V/VI. No cortical or brainstem Lewy bodies (assessed by α-synuclein IHC) were present. There was only minimal cortical gliosis, and no infarcts in subcortical or cortical structures. Immunohistochemical analyses demonstrated frequent Aβ immunoreactive plaques and mild amyloid angiopathy. Bielschowsky staining revealed frequent SP and NFT in all neocortical areas; this was confirmed with IHC using the anti-phosphotau antibody clone AT8.

Post-mortem measures of 6-CN-PiB and Aβ plaque loads, AT8-immunoreactive neurofibrillary load and [^{3}H]PiB binding were quantified in tissue sections cut from the 25 tissue cubes in a 1-cm thick tissue slab from the formalin-fixed left hemisphere. The final analysis included values from 19 tissue cubes (the MRI VOI of six of the 25 tissue cubes contained <70% tissue and were excluded, see Methods section); these values were correlated with the PiB-PET DVR values from the 19 corresponding VOIs on the ante-mortem PET scans at the same axial level of the same hemisphere in this person, after correction for any partial volume effects (see Methods section). At this brain level, the highest values for 6-CN-PiB plaque load were observed in the frontal and temporal cortices, and in the basal ganglia. The lowest 6-CN-PiB plaque load levels were in the tail of the hippocampus, internal capsule and lateral occipital cortex (Fig. 4). This distribution of 6-CN-PiB plaque load values was similar to the distribution of PiB DVR values in the same brain regions on the matching ante-mortem PiB-PET scan (Fig. 5). Figure 4 illustrates the pattern of 6-CN-PiB labelling and the extent of X-34 labelled amyloid pathology, 6E10 immunoreactive Aβ plaques and AT8 immunoreactive neurofibrillary pathology, in adjacent tissue sections from three tissue cubes representative of brain areas with either high-plaque/high-NFT density (cube #16, frontal cortex), high plaque/low NFT (cube #1, striatum) or low-plaque/high-NFT density (cube #25, hippocampus). 6-CN-PiB labelling corresponded well with Aβ plaques revealed by 6E10 IHC, but not with NFT density as revealed by AT8 IHC (Fig. 4). The overall X-34 labelling load, which reveals all β-sheet deposits including Aβ plaques and neurofibrillary pathology (NFT, DN and NT) (Ikonomovic *et al.*, 2006), did not correspond as well to 6-CN-PiB labelling as did 6E10 IHC for Aβ alone. However, after restricting the analysis to include only X-34 labelled plaques, there was a good correlation between 6-CN-PiB and X-34 plaque load. There was a direct correlation ($r = 0.81$, $P < 0.0001$) of 6-CN-PiB fluorescent plaque load determined post-mortem with *in vivo* PiB retention (Figs 5 and 6A). A similar direct correlation was found between *in vivo* PiB DVR values and Aβ immunoreactive plaque load (Fig. 6B). In contrast, there was no correlation between *in vivo* PiB DVR values and the neurofibrillary pathology load as revealed by AT8 IHC (Fig. 6C).

Aβ peptide levels could not be quantified by ELISA in the formalin-fixed tissue homogenate. However, specific, displaceable [^{3}H]PiB binding could be detected in this formalin-fixed tissue. There was a strong significant correlation ($r = 0.82$, $P < 0.0001$) between [^{3}H]PiB binding to homogenates of post-mortem formalin-fixed tissue and PiB DVR values from ante-mortem PET scans (Fig. 6D). In a separate validation study of six Alzheimer's disease brains from our autopsy series, we examined [^{3}H]PiB binding in tissues bisected from frontal and occipital cortical samples; half of each sample was formalin-fixed for three days (to reproduce the effects of formalin-fixation on the autopsied brain in the PiB-PET Alzheimer's disease case study) and the other half was fresh frozen. Although there was a good correlation between [^{3}H]PiB binding to the formalin-fixed

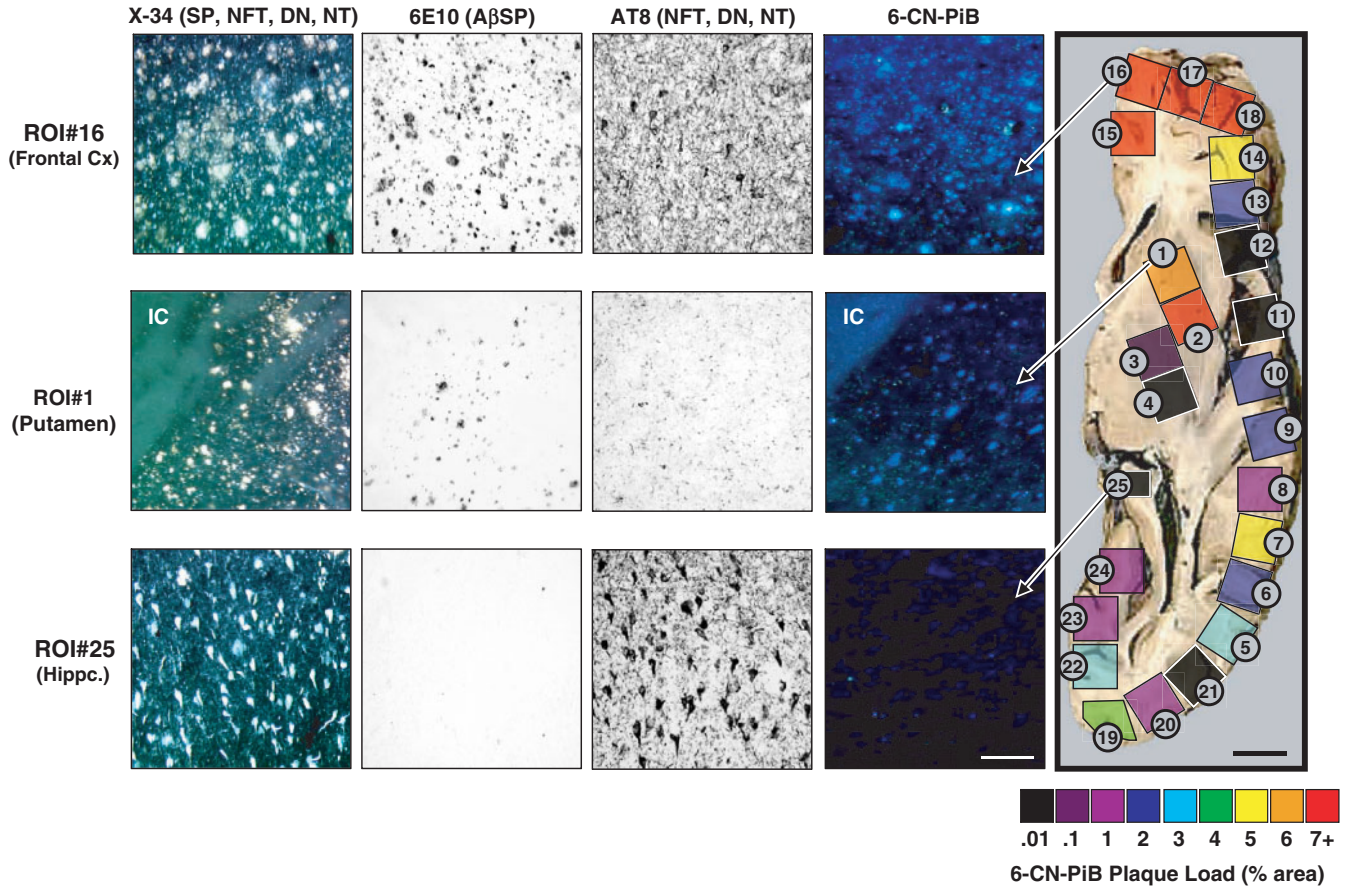

Fig. 4 6-CN-PiB plaque load (% area) values, quantified in each of the 25 tissue cubes dissected from an axial post-mortem tissue block, are pseudo-colour-coded on a rainbow scale from black/purple (low% area) to red (high% area). Images of 6-CN-PiB and X-34 histofluorescence, and 6E10 and AT8 IHC, were obtained in adjacent tissue sections from tissue cube #16 (frontal cortex), tissue cube #1 (striatum) and tissue cube #25 (hippocampus), and are each representative of an area with highest concentrations of labelled elements. In all tissue cubes, 6-CN-PiB exclusively labels plaques, matching the distribution of 6E10 immunoreactive and X-34 labelled plaques, but not AT8 immunoreactive or X-34 labelled NFT, DN and NT. Abbreviations: IC = internal capsule (low background fluorescence in the white matter tracts); NFT = neurofibrillary tangles; DN = dystrophic neurites; NT = neuropil threads; Hippc = hippocampus; Cx = cortex. Scale bar = 150 μm for tissue cube #16 and #1, 75 μm for tissue cube #25 and 1 cm for tissue slab.

and frozen samples ($r = 0.66$; $P = 0.038$), the binding of [^{3}H]PiB to the formalin-fixed samples was only 43 ± 24% of that observed in the corresponding frozen tissue samples. Therefore, we also measured [^{3}H]PiB binding in fresh-frozen tissue samples from 14 brain regions dissected from the contralateral (frozen) hemisphere of the PiB-PET-scanned Alzheimer's disease case. Although the co-localization of the VOI used to determine the *in vivo* DVR value and the frozen tissue used to measure [^{3}H]PiB binding could not be performed as exactly as it could on the formalin-fixed tissue, there also was a strong correlation of [^{3}H]PiB binding with *in vivo* PiB retention DVR levels in the frozen tissue ($r = 0.64$, $P = 0.013$, Fig. 6E).

In the same 14 fresh-frozen tissue samples from the right hemisphere, we next quantified Aβ40 and Aβ42 peptide levels for correlations with region-matched *in vivo* PiB retention DVR values and *in vitro* [^{3}H]PiB binding. There was a strong correlation of *in vivo* PiB retention levels with tissue levels of total (i.e. Aβ40 + Aβ42) insoluble Aβ ($r = 0.73$, $P < 0.0028$, Fig. 6F). As observed in frozen frontal and occipital cortex tissue homogenates from six Alzheimer's disease subjects in our autopsy series (Supplementary Fig. 4B), in the 14 frozen tissue homogenates from the PiB-PET scanned Alzheimer's disease case there was a strong correlation of *in vitro* [^{3}H]PiB binding with total (i.e. Aβ40 + Aβ42) insoluble Aβ ($r = 0.85$, $P = 0.0001$, Supplementary Fig. 5A). These biochemical results were supported by a strong correlation between histological 6-CN-PiB plaque load and 6E10 immunoreactive Aβ plaque load in the tissue cubes dissected from the formalin fixed hemisphere ($r = 0.86$; $P < 0.0001$; Supplementary Fig. 5B).

Discussion

We have defined the histological and biochemical specificity of PiB binding across different regions of Alzheimer's disease brain, and demonstrated a direct correlation

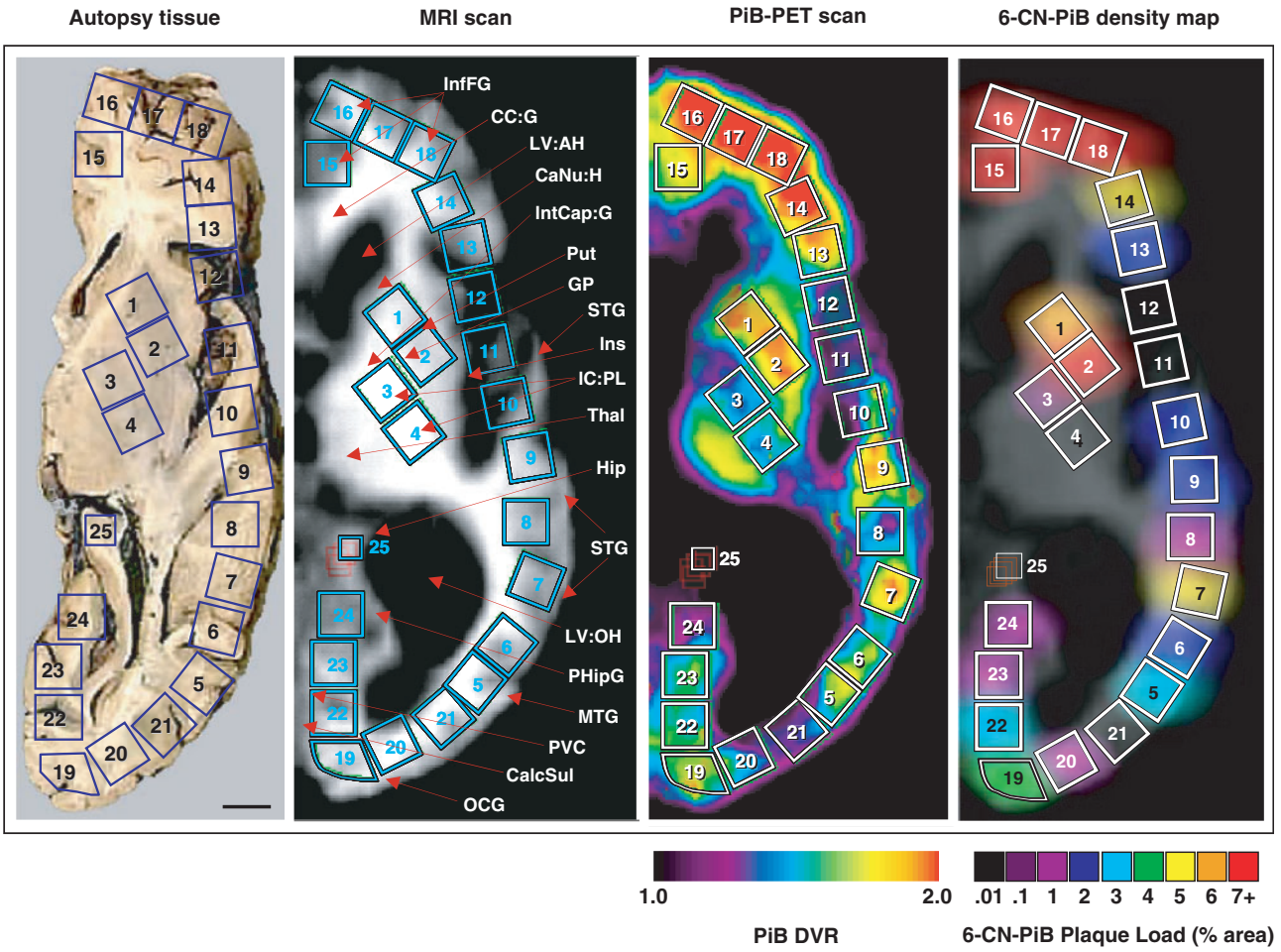

Fig. 5 Correlation between ante-mortem PiB-PET retention levels and a post-mortem VOI-matched 6-CN-PiB plaque density map as a 'virtual PiB scan' of the same subject. The face of the autopsy tissue block is at the level of the anterior and posterior commisures. On the autopsy tissue (left) each of the 25 blue squares represents the face of a tissue cube that was dissected from this 1-cm formalin-fixed slab. ROIs corresponding to these 25 tissue cubes were drawn on the corresponding four 0.24-cm slices of this same patient's MRI scan (second from the left; taken at the time of the PiB scan 10 months before death). These same ROIs were then transferred to the co-registered PiB-PET scan (third from left) for quantification of the *in vivo* PiB retention. Some tissue distortion post-mortem is evident, due to the collapse of the ventricles. On the 6-CN-PiB density map (right), the data from the post-mortem regional 6-CN-PiB plaque load analysis (see Fig. 4) were digitally blurred to create the 'virtual PiB scan', shown overlying the contour of the MRI scan for ROI comparison purposes. This post-mortem 6-CN-PiB plaque density map closely reflects the distribution of PiB retention levels in the PiB-PET scan recorded ante-mortem in the same person. Abbreviations: InfFG = inferior frontal gyrus; CC:G = corpus callosum: genu; LV:AH = lateral ventricle: anterior horn; CaNu:H = caudate nucleus: head; IntCap:G = internal capsule: genu; Put = putamen; GP = globus pallidus; STG = superior temporal gyrus; Ins = insular cortex; IC:PL = internal capsule: posterior limb; Thal = thalamus; Hip = hippocampus; STG = superior temporal gyrus; LV:OH = lateral ventricle: occipital horn; PHipG = parahippocampal gyrus; MTG = medial temporal gyrus; PVC = primary visual cortex; CalcSul = calcarine sulcus; OCG = occipital gyrus. Scale bar = 1 cm.

between Aβ containing amyloid plaques and *in vivo* PiB retention measured by PET imaging. The highly fluorescent PiB analogue, 6-CN-PiB, almost exclusively labelled Aβ-containing structures including compact/cored, diffuse, neuritic and non-neuritic Aβ plaques. 6-CN-PiB also labelled vascular amyloid, as previously reported (Bacskai *et al.*, 2007; Lockhart *et al.*, 2007), but fluorescence signal was not detected in neuropil threads or dystrophic neurites, and only sporadically in a subset of NFT; these were primarily of extracellular 'ghost' tangle (eNFT) morphology. Our study of an Alzheimer's disease subject who underwent post-mortem neuropathological examination 10 months after *in vivo* PiB-PET imaging, demonstrated that *in vivo* PiB retention correlated directly with region-matched post-mortem quantification of 6-CN-PiB and Aβ plaque load, PiB binding and Aβ peptide levels, but not NFT or other neurofibrillary pathology. Although the PiB-PET study and autopsy were separated by 10 months, Engler *et al.* (2006) have shown that PiB-PET DVR values do not change appreciably over 2 years in patients with Alzheimer's disease.

The close co-localization of 6-CN-PiB labelling with Aβ40 and Aβ42 immunoreactive plaques, and the *in vitro* binding of [^{3}H]PiB to synthetic fibrils made from either

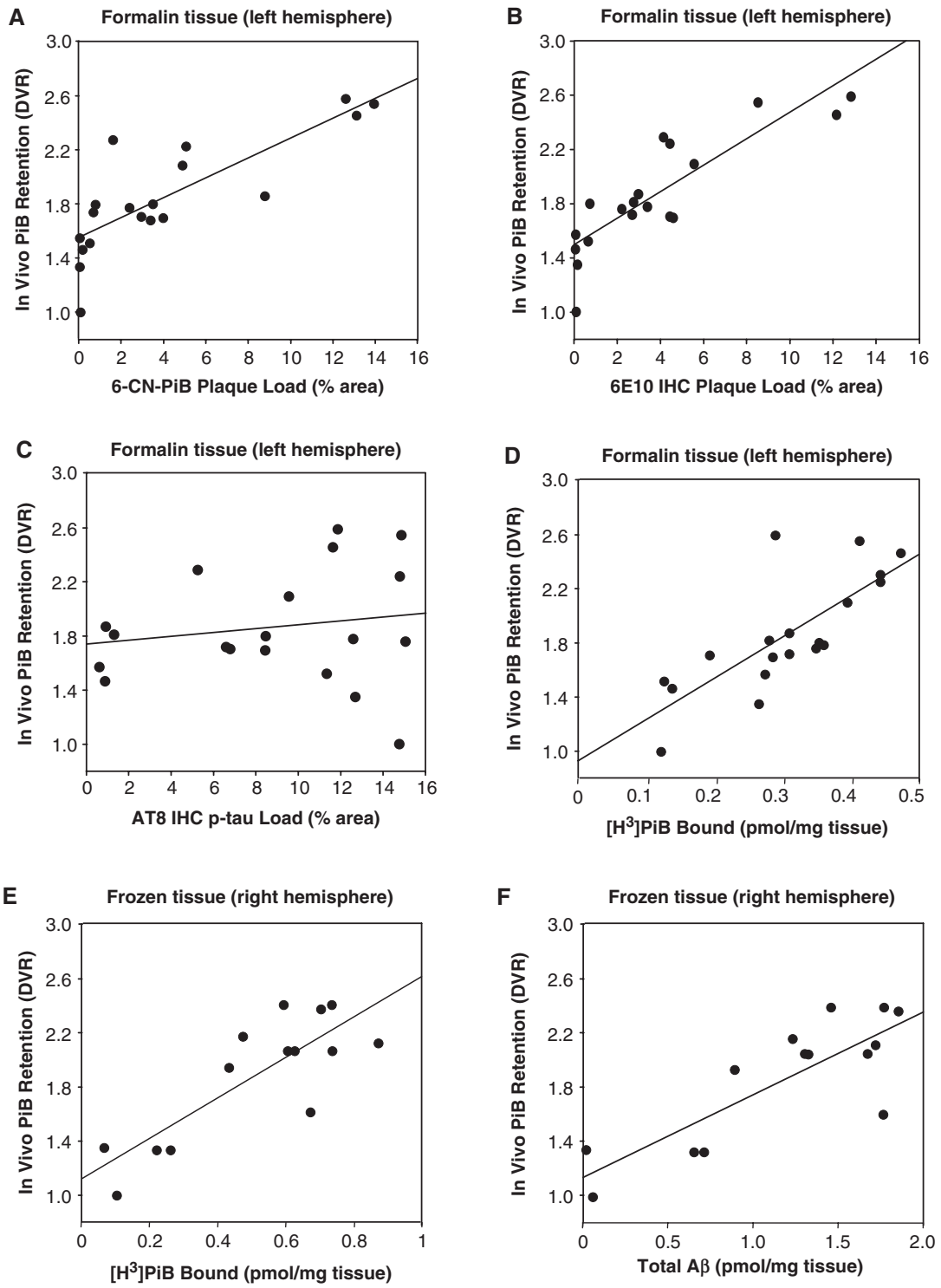

Fig. 6 Correlations of the *in vivo* PiB DVR values from the 19 VOIs (six of the 25 VOIs had <70% tissue and were not included in the analysis, see Methods section) on the PET scan with post-mortem quantifications of 6-CN-PiB (**A**) or Aβ (**B**) plaque load, neurofibrillary load (**C**) and [^{3}H]PiB binding (**D**) in the corresponding 19 tissue cubes from the formalin fixed left hemisphere. *In vivo* PiB-PET retention (DVR) levels correlate directly with regional post-mortem quantitations of 6-CN-PiB (**A**) and 6E10 (**B**) plaque loads as well as *in vitro* PiB binding (**D**), but not with AT8 neurofibrillary load (**C**) in formalin-fixed tissue from the left hemisphere. In fresh-frozen tissue from the right hemisphere of the same Alzheimer's disease subject, there is a significant correlation of both *in vitro* PiB binding (**E**) and total insoluble Aβ ($A\beta_{1-40} + A\beta_{1-42}$) peptide levels (**F**) with *in vivo* PiB-PET retention (DVR) levels.

$A\beta_{1-40}$ or $A\beta_{1-42}$, indicate that PiB binds similarly to these two forms of Aβ, once they have adopted a β-sheet fibrillar structure. Aβ42-containing plaques and Aβ42 peptide levels are much more abundant in Alzheimer's disease brain (Iwatsubo *et al.*, 1994; Naslund *et al.*, 2000), and therefore likely drive the correlation between PiB and total Aβ peptide (Aβ42 and Aβ40 combined) levels as determined in our ELISA assays. Thus, the majority of *in vivo* PiB retention on PET scans in Alzheimer's disease reflects aggregated Aβ42 deposits. We did not explore the effect of the Aβ N-terminal heterogeneity on PiB binding, but a recent paper examining PiB binding to brain tissue from transgenic mouse models of amyloid deposition suggested that the form of Aβ starting with cyclized glutamate in the 3-position [i.e. pyroglutamate or N3(pE) form] is a major contributor to PiB binding (Maeda *et al.*, 2007). This is of interest given the previously reported findings that the N3(pE) form of Aβ comprises 25–50% of total Aβ (Harigaya *et al.*, 2000; Russo *et al.*, 2002).

The requirement that Aβ be in fibrillar form for PiB binding was verified both by the demonstration that formic acid pre-treatment of tissue sections (which disrupts the β-sheet fibrillar structure) abolished 6-CN-PiB binding to plaques and vascular amyloid, and by the direct correlation of *in vitro* PiB binding with insoluble (formic acid extracted) Aβ which forms amyloid plaques, but not with soluble Aβ. The intensity of 6-CN-PiB plaque labelling reflected the density of Aβ immunoreactive fibrils in plaques, from lightly labelled diffuse plaques to intensely fluorescent compact/cored plaques.

The only region that lacked the close correlation between 6-CN-PiB fluorescence labelling and Aβ immunoreactivity in plaques was the cerebellum. The rare, small compact plaques in the Purkinje and granular layers, and infrequent CAA were labelled by 6-CN-PiB. However, fleecy appearing diffuse plaques in the molecular layer (the vast majority of Aβ immunoreactive and X-34 positive plaques in the cerebellum) were not detectable with 6-CN-PiB. This is consistent with the observation that *in vivo* PiB retention levels in Alzheimer's disease brain are consistently lowest in the cerebellum, and further justifies using the cerebellum as a reference region when quantifying regional *in vivo* PiB retention levels (Lopresti *et al.*, 2005).

The binding of PiB to diffuse plaques in the striatum and other regions examined, but not in the cerebellum, is likely due to the unique secondary structure and amino acid composition of cerebellar diffuse Aβ aggregates (Lalowski *et al.*, 1996). Furthermore, unlike the occasional small compact plaques that were 6-CN-PiB positive, cerebellar diffuse plaques contain few amyloid fibrils characteristic of plaque cores (Verga *et al.*, 1989). The intense 6-CN-PiB labelling of all compact cored plaques, the weaker labelling of diffuse cortical, striatal and hippocampal plaques, and the complete absence of labelling in cerebellar fleecy amyloid may be due to higher amyloid fibril density in the compact cored plaques. 6-CN-PiB did not label dystrophic neurites, indicating that plaque-associated neuritic elements do not likely contribute to overall PiB signal, despite the robust labelling of these structures with other amyloid-binding compounds such as X-34. Because PiB can detect diffuse plaques in addition to cored and neuritic plaques, PiB-PET imaging may be useful for detection of early amyloid deposition. PiB-PET is able to track Aβ deposition across the spectrum of normal aging to advanced Alzheimer's disease (Forsberg *et al.*, 2007; Kemppainen *et al.*, 2007; Rowe *et al.*, 2007), and further histological studies will need to be performed to assess the relative contributions of different plaque types across this spectrum. Compact Aβ plaques are likely associated with increased presence of reactive glial cells. It will be important to examine correlations of PiB binding with microglial and astrocytic activation, as well as additional cellular and molecular alterations, in future studies.

In contrast to the strong correlation between 6-CN-PiB staining and Aβ plaques, 6-CN-PiB did not bind at detectable levels to significant numbers of NFT, even in the ERC layer II cell islands where tau-immunoreactive and X-34 fluorescent NFT were abundant. This is consistent with the previously reported observation in elderly healthy control brain of a lack of [^{3}H]PiB binding to homogenates of transentorhinal cortex (Klunk *et al.*, 2003*b*), a brain area that is the first to show NFT pathology (Braak and Braak, 1991*a*). These observations differ somewhat from those of Lockhart *et al.* (2007), who reported overlap between NFT-labelling and PiB autoradiography in the ERC. The finding by Lockhart *et al.* could be the result of long autoradiography exposure time (7 weeks) wherein even the weakest signal can be amplified, or it could be due to misidentification of structures due to the low resolution of film autoradiography, as well as comparison of different tissue sections (as opposed to multiple labelling on single tissue section). In the present study, we did observe weak PiB labelling of a relatively small subset of NFT, mostly extracellular NFT detectable in the ERC layer II and subiculum/CA1, while the majority of intracellular NFT were not detectable. This pattern was confirmed by additional histological experiments using another fluorescent PiB derivative, BTA-1 (see Supplementary Fig. 2). In the ERC lamina II, the bulk of NFT were BTA-1 negative, while small-diameter plaques were BTA-1 positive. This distinction would not have been detected by the autoradiographic approach used by Lockhart *et al.* (2007). Furthermore, in the Lockhart *et al.* study (Lockhart *et al.*, 2007), some N-terminus Aβ truncated diffuse Aβ plaques in the ERC could have gone undetected by the N-terminus Aβ IHC and thioflavin-S histochemistry. Since select NFT, and particularly extracellular NFT, contain epitopes recognized by Aβ antibodies (Masters *et al.*, 1985; Grundke-Iqbal *et al.*, 1989; Hyman *et al.*, 1989; Spillantini *et al.*, 1990; Tabaton *et al.*, 1991; Perry *et al.*, 1993), we must also consider the possibility that the NFT labelled by 6-CN-PiB and BTA-1 represent NFT-associated Aβ peptides that fibrilized once

the NFT became extracellular (Grundke-Iqbal *et al.*, 1989). Thus, even the occasional labelling of extracellular NFT observed in this study may be due to the presence of Aβ fibrils, rather than the presence of high-affinity binding sites on tau-formed amyloid (Lockhart *et al.*, 2007). Alternatively, extracellular proteolysis of tau in extracellular NFT may expose the protease-resistant core of PHF, or change its structure (Mena *et al.*, 1995, 1996) making it accessible to PiB. Regardless, the binding of PiB to a subset of NFT produces weak signal relative to that generated by PiB-bound Aβ plaques, and does not likely contribute significantly to tracer uptake and PiB-PET signal *in vivo*. This is supported by the fact that *in vivo* PiB-PET imaging studies consistently demonstrated very little signal in mesial temporal lobe, despite the high NFT load detected both histologically and immunohistochemically in this region (see Figs 4 and 5). It should also be noted that the presence of the cell membrane is not likely the determining factor for PiB labelling differences between intracellular and extracellular NFT because: (i) the cell membrane is not likely to be intact in the histological sections; and (ii) PiB has to cross several membranes which comprise the blood–brain barrier in order to access either plaques or NFT *in vivo*.

In this study, the strong labelling of CAA (when present) by 6-CN-PiB was of similar intensity to compact plaques, but the frequency of CAA in the typical Alzheimer's disease brains we examined was much lower than that of plaques. Thus in most Alzheimer's disease subjects, PiB binding to CAA contributes relatively little to the total *in vivo* signal, which appears to be driven primarily by Aβ-containing amyloid plaques. In subjects with amyloid angiopathy (Johnson *et al.*, 2007) CAA could be a major contribution to the *in vivo* PiB signal. However, CAA pathology has an occipital predilection, resulting in a greater occipital-to-global PiB ratio compared to Alzheimer's disease patients (Johnson *et al.*, 2007). This underscores the need to interpret the PiB-PET imaging relative to the known occurrence of neuropathological lesions in the brain areas under investigation.

Until recently, it was not possible to establish a direct relationship between PiB retention *in vivo* and Aβ pathology in the same subject. In a case of pathologically confirmed dementia with Lewy bodies and severe CAA (Bacskai *et al.*, 2007), ante-mortem PiB retention levels correlated with post-mortem biochemical measures of Aβ and PiB binding in three brain regions. PiB binding in this case was primarily associated with vascular Aβ deposits due to the CAA, while Aβ plaques were scarce. This made it difficult to directly correlate *in vivo* PiB retention with Aβ plaque deposits in that case, and no correlation was attempted with histological or immunohistochemical Aβ load. Nevertheless, the results of that study suggested a correlation between *in vivo* PiB measures with Aβ amyloid load, and thus are in accord with the present study, which clearly demonstrates that *in vivo* PiB retention in a pathologically typical Alzheimer's disease patient is related directly to the amount of insoluble Aβ peptides, including Aβ plaques.

Our results underscore the validity of using PiB-PET scanning not only to detect and follow the progression of Aβ-containing fibrillar amyloid deposits in clinically defined subject populations, but also to assess effectiveness of therapies aimed at clearing these potentially toxic deposits from the brain.

Supplementary material

Supplementary material is available at *Brain* online.

Acknowledgements

This work was funded by National Institutes of Health (R01 AG018402 to C.A.M., P50 AG05133 to S.T.DeK., P01 AG14449 to S.T.DeK., K02 AG001039 to W.E.K., R01 AG020226 to W.E.K., R01 MH070729 to J.C.P., K01 MH001976 to J.C.P., R37 AG025516 to W.E.K., P01 AG025204 to S.T.DeK.); The Alzheimer's Association (TLL-01-3381 to W.E.K.); The U.S. Department of Energy (DE-FD02-03 ER63590 to C.A.M.); The Dana Foundation (to J.C.P. and C.A.M.). We thank the staff at the University of Pittsburgh Alzheimer's Disease Research Center and PET facility for their efforts in conducting and analysing these studies. We are indebted to our subjects and their families for the selfless contributions that made this work possible. Funding to pay the Open Access publication charges for this article was provided by NIH grants AG05133 and AG025516.

References

Consensus report of the Working Group on "Molecular and Biochemical Markers of Alzheimer's Disease". The Ronald and Nancy Reagan Research Institute of the Alzheimer's Association and the National Institute on Aging Working Group. Neurobiol Aging 1998; 19: 109–16.

Bacskai BJ, Frosch MP, Freeman SH, Raymond SB, Augustinack JC, Johnson KA, et al. Molecular imaging with PiB confirmed at autopsy: a case report. Arch Neurol 2007; 64: 431–4.

Braak H, Braak E. Neuropathological stageing of Alzheimer-related changes. Acta Neuropath 1991a; 82: 239–59.

Braak H, Braak E. Neuropathological staging of Alzheimer's disease. Acta Neuropath 1991b; 82: 239–59.

DeKosky ST, Abrahamson EE, Ciallella JR, Paljug WR, Wisniewski SR, Clark RSB, et al. Association of increased cortical soluble abeta42 levels with diffuse plaques after severe brain injury in humans. Arch Neurol 2007; 64: 541–44.

Engler H, Forsberg A, Almkvist O, Blomquist G, Larsson E, Savitcheva I, et al. Two-year follow-up of amyloid deposition in patients with Alzheimer's disease. Brain 2006; 129: 2856–66.

Fodero-Tavoletti MT, Smith DP, McLean CA, Adlard PA, Barnham KJ, Foster LE, et al. In vitro characterization of Pittsburgh compound-B binding to Lewy bodies. J Neurosci 2007; 27: 10365–71.

Forsberg A, Engler H, Almkvist O, Blomquist G, Hagman G, Wall A, et al. PET imaging of amyloid deposition in patients with mild cognitive impairment. Neurobiol Aging 2007 [Epub ahead of print] (doi: 10.1016/j.neurobiolaging.2007.03.029).

Gauthier S, Reisberg B, Zaudig M, Petersen RC, Ritchie K, Broich K, et al. Mild cognitive impairment. Lancet 2006; 367: 1262–70.

Growdon JH. Biomarkers of Alzheimer disease. Arch Neurol 1999; 56: 281–3.

Grundke-Iqbal I, Iqbal K, George L, Tung YC, Kim KS, Wisniewski HM. Amyloid protein and neurofibrillary tangles coexist in the same neuron in Alzheimer disease. Proc Natl Acad Sci USA 1989; 86: 2853–57.

Guntern R, Bouras C, Hof PR, Vallet PG. An improved thioflavine-S method for staining neurofibrillary tangles and senile plaques in Alzheimer's disease. Experientia 1992; 48: 8–10.

Harigaya Y, Saido TC, Eckman CB, Prada CM, Shoji M, Younkin SG. Amyloid beta protein starting pyroglutamate at position 3 is a major component of the amyloid deposits in the Alzheimer's disease brain. Biochem Biophys Res Commun 2000; 276: 422–27.

Hyman BT, Tanzi RE, Marzloff K, Barbour R, Schenk D. Kunitz protease inhibitor-containing amyloid beta protein precursor immunoreactivity in Alzheimer's disease. J Neuropathol Exp Neurol 1992; 51: 76–83.

Hyman BT, Van Hoesen GW, Beyreuther K, Masters CL. A4 amyloid protein immunoreactivity is present in Alzheimer's disease neurofibrillary tangles. Neurosci Lett 1989; 101: 352–55.

Ikonomovic MD, Abrahamson EE, Isanski BA, Debnath ML, Mathis CA, DeKosky ST, et al. X-34, a histofluorescent marker of abnormal protein aggregates with amyloid structure, in neuropathological studies of preclinical and clinical Alzheimer's disease. Methods Enzymol 2006; 412: 123–44.

Iwatsubo T, Odaka A, Suzuki N, Mizusawa H, Nukina N, Ihara Y. Visualization of Aβ42(43) and Aβ40 in senile plaques with end-specific Aβ monoclonals: Evidence that an initially deposited species is Aβ42(43). Neuron 1994; 13: 45–53.

Johnson KA, Gregas M, Becker JA, Kinnecom C, Salat DH, Moran EK, et al. Imaging of amyloid burden and distribution in cerebral amyloid angiopathy. Ann Neurol 2007; 62: 229–34.

Kamal A, Almenar-Queralt A, LeBlanc JF, Roberts EA, Goldstein LS. Kinesin-mediated axonal transport of a membrane compartment containing beta-secretase and presenilin-1 requires APP. Nature 2001; 414: 643–8.

Kemppainen NM, Aalto S, Wilson IA, Nagren K, Helin S, Bruck A, et al. PET amyloid ligand [11C]PIB uptake is increased in mild cognitive impairment. Neurology 2007; 68: 1603–06.

Khachaturian ZS. Diagnosis of Alzheimer's disease. Arch Neurol 1985; 42: 1097–105.

Kim K, Wen G, Bancher C, Chen CMJ, Sapienza VJ, Hong H, et al. Detection and quantification of β-peptide with two monoclonal antibodies. Neurosci Res Commun 1990; 7: 113–22.

Kitamoto T, Ogomori K, Tateishi J, Prusiner SB. Formic acid pretreatment enhances immunostaining of cerebral and systemic amyloids. Lab Invest 1987; 57: 230–6.

Klunk WE. Biological markers of Alzheimer's disease. Neurobiol Aging 1998; 19: 145–47.

Klunk W, Engler H, Nordberg A, Bacskai BJ, Wang Y, Price JC, et al. Imaging the pathology of Alzheimer's disease: amyloid imaging with positron emission tomography. Neuroimaging Clin N Am 2003a; 13: 781–9.

Klunk WE, Engler H, Nordberg A, Wang Y, Blomqvist G, Holt DP, et al. Imaging brain amyloid in Alzheimer's disease with Pittsburgh Compound-B. Ann Neurol 2004; 55: 306–19.

Klunk WE, Lopresti BJ, Ikonomovic MD, Lefterov IM, Koldamova RP, Abrahamson EE, et al. Binding of the positron emission tomography tracer Pittsburgh compound-B reflects the amount of amyloid-beta in Alzheimer's disease brain but not in transgenic mouse brain. J Neurosci 2005; 25: 10598–606.

Klunk WE, Wang Y, Huang GF, Debnath ML, Holt DP, Mathis CA. Uncharged thioflavin-T derivatives bind to amyloid-beta protein with high affinity and readily enter the brain. Life Sci 2001; 69: 1471–84.

Klunk W, Yanming W, Huang G-F, Debnath ML, Holt DP, Shao L, et al. The binding of BTA-1 to post-mortem brain homogenates is dominated by amyloid component. J Neurosci 2003b; 23: 2086–92.

Lalowski M, Golabek A, Lemere CA, Selkoe DJ, Wisniewski HM, Beavis RC, et al. The ''nonamyloidogenic'' p3 fragment (amyloid beta17-42) is a major constituent of Down's syndrome cerebellar preamyloid. J Biol Chem 1996; 271: 33623–31.

Lammertsma AA, Hume SP. Simplified reference tissue model for PET receptor studies. Neuroimage 1996; 4: 153–58.

Lockhart A, Lamb JR, Osredkar T, Sue LI, Joyce JN, Ye L, et al. PIB is a non-specific imaging marker of amyloid-beta (Abeta) peptide-related cerebral amyloidosis. Brain 2007; 130: 2607–15.

Logan J, Fowler JS, Volkow ND, Wang GJ, Ding YS, Alexoff DL. Distribution volume ratios without blood sampling from graphical analysis of PET data. J Cereb Blood Flow Metab 1996; 16: 834–40.

Lopez OL, Becker JT, Klunk W, Saxton J, Hamilton RL, Kaufer DI, et al. Research evaluation and diagnosis of possible Alzheimer's disease over the last two decades: II. Neurology 2000a; 55: 1863–69.

Lopez OL, Becker JT, Klunk W, Saxton J, Hamilton RL, Kaufer DI, et al. Research evaluation and diagnosis of probable Alzheimer's disease over the last two decades: I. Neurology 2000b; 55: 1854–62.

Lopresti BJ, Klunk WE, Mathis CA, Hoge JA, Ziolko SK, Lu X, et al. Simplified quantification of Pittsburgh Compound B amyloid imaging PET studies: a comparative analysis. J Nucl Med 2005; 46: 1959–72.

Maeda J, Ji B, Irie T, Tomiyama T, Maruyama M, Okauchi T, et al. Longitudinal, quantitative assessment of amyloid, neuroinflammation, and anti-amyloid treatment in a living mouse model of Alzheimer's disease enabled by positron emission tomography. J Neurosci 2007; 27: 10957–968.

Masters CL, Multhaup G, Simms G, Pottgiesser J, Martins RN, Beyreuther K. Neuronal origin of a cerebral amyloid: neurofibrillary tangles of Alzheimer's disease contain the same protein as the amyloid of plaque cores and blood vessels. EMBO J 1985; 4: 2757–63.

Mathis CA, Bacskai BJ, Kajdasz ST, McLellan ME, Frosch MP, Hyman BT, et al. A lipophilic thioflavin-T derivative for positron emission tomography (PET) imaging of amyloid in brain. Bioorg Med Chem Lett 2002; 12: 295–98.

Mathis CA, Klunk WE, Price JC, DeKosky ST. Imaging technology for neurodegenerative diseases: progress toward detection of specific pathologies. Arch Neurol 2005; 62: 196–200.

Mathis C, Wang Y, Holt D, Huang G-F, Debnath ML, Klunk WE. Synthesis and evaluation of 11C-labeled 6-substituted 2-aryl benzothiazoles as amyloid imaging agents. J Med Chem 2003; 46: 2740–55.

Mathis C, Wang Y, Klunk W. Imaging beta-amyloid plaques and neurofibrillary tangles in the aging human brain. Curr Pharma Design 2004; 10: 1469–92.

Mayeux R, Saunders AM, Shea S, Mirra S, Evans D, Roses AD, et al. Utility of the apolipoprotein E genotype in the diagnosis of Alzheimer's disease. Alzheimer's Disease Centers Consortium on Apolipoprotein E and Alzheimer's Disease. N Engl J Med 1998; 338: 506–11.

McKhann G, Drachman D, Folstein M, Katzman R, Price D, Stadlan EM. Clinical diagnosis of Alzheimer's disease: Report of Health and Human Services Task Force on Alzheimer's Disease. Neurology 1984; 34: 939–44.

Meltzer CC, Kinahan PE, Greer PJ, Nichols TE, Comtat C, Cantwell MN, et al. Comparative evaluation of MR-based partial-volume correction schemes for PET. J Nucl Med 1999; 40: 2053–65.

Mena R, Edwards PC, Harrington CR, Mukaetova-Ladinska EB, Wischik CM. Staging the pathological assembly of truncated tau protein into paired helical filaments in Alzheimer's disease. Acta Neuropathol (Berl) 1996; 91: 633–41.

Mena R, Edwards P, Perez-Olvera O, Wischik CM. Monitoring pathological assembly of tau and beta-amyloid proteins in Alzheimer's disease. Acta Neuropathol 1995; 89: 50–6.

Mercken M, Vandermeeren M, Lubke U, Six J, Boons J, Van de Voorde A, et al. Monoclonal antibodies with selective specificity for Alzheimer Tau are directed against phosphatase-sensitive epitopes. Acta Neuropathol 1992; 84: 265–72.

Mintun MA, Raichle ME, Kilbourn MR, Wooten GF, Welch MJ. A quantitative model for the in vivo assessment of drug binding sites with positron emission tomography. Ann Neurol 1984; 15: 217–27.

Mirra SS, Heyman A, McKeel D, Sumi SM, Crain BJ, Brownlee LM, et al. The consortium to establish a registry for Alzheimer's disease

(CERAD). Part II. Standardization of the neuropathologic assessment of Alzheimer's disease. Neurology 1991; 41: 479–86.

Morris JC, Kimberly A, Quaid K, Holtzman DM, Kantarci K, Kaye J, et al. Role of biomarkers in studies of presymptomatic Alzheimer's disease. Alzheimer Dem 2005; 1: 145.

Naslund J, Haroutunian V, Mohs R, Davis KL, Davies P, Greengard P, et al. Correlation between elevated levels of amyloid β-peptide in the brain and cognitive decline. JAMA 2000; 283: 1571–77.

Nicoll JA, Barton E, Boche D, Neal JW, Ferrer I, Thompson P, et al. Abeta species removal after abeta42 immunization. J Neuropathol Exp Neurol 2006; 65: 1040–48.

Pearl GS. Diagnosis of Alzheimer's disease in a community hospital-based brain bank program. South Med J 1997; 90: 720–22.

Perry G, Richey PL, Siedlak SL, Smith MA, Mulvihill P, Dewitt DA, et al. Immunocytochemical evidence that the beta-protein precursor is an integral component of neurofibrillary tangles of Alzheimers Disease. Am J Pathol 1993; 143: 1586–93.

Price JC, Klunk WE, Lopresti BJ, Lu X, Hoge JA, Ziolko SK, et al. Kinetic modeling of amyloid binding in humans using PET imaging and Pittsburgh Compound-B. J Cereb Blood Flow Metab 2005; 25: 1528–47.

Rowe CC, Ng S, Ackermann U, Gong SJ, Pike K, Savage G, et al. Imaging beta-amyloid burden in aging and dementia. Neurology 2007; 68: 1718–25.

Russo C, Violani E, Salis S, Venezia V, Dolcini V, Damonte G, et al. Pyroglutamate-modified amyloid beta-peptides–AbetaN3(pE)–strongly affect cultured neuron and astrocyte survival. J Neurochem 2002; 82: 1480–89.

Small GW, Kepe V, Ercoli LM, Siddarth P, Bookheimer SY, Miller KJ, et al. PET of brain amyloid and tau in mild cognitive impairment. N Engl J Med 2006; 355: 2652–63.

Spillantini MG, Goedert M, Jakes R, Klug A. Topographical relationship between beta-amyloid and tau protein epitopes in tangle-bearing cells in Alzheimer disease. Proc Natl Acad Sci USA 1990; 87: 3952–56.

Tabaton M, Cammarata S, Mancardi G, Manetto V, Autilio-Gambetti L, Perry G, et al. Ultrastructural localization of beta-amyloid, tau, and ubiquitin epitopes in extracellular neurofibrillary tangles. Proc Natl Acad Sci USA 1991; 88: 2098–102.

Thal LJ, Kantarci K, Reiman EM, Klunk WE, Weiner MW, Zetterberg H, et al. The role of biomarkers in clinical trials for Alzheimer disease. Alzheimer Dis Assoc Disord 2006; 20: 6–15.

Thies E, Mandelkow EM. Missorting of tau in neurons causes degeneration of synapses that can be rescued by the kinase MARK2/Par-1. J Neurosci 2007; 27: 2896–907.

Verga L, Frangione B, Tagliavini F, Giaccone G, Migheli A, Bugiani O. Alzheimer patients and Down patients: cerebral preamyloid deposits differ ultrastructurally and histochemically from the amyloid of senile plaques. Neurosci Lett 1989; 105: 294–99.

Verhoeff NP, Wilson AA, Takeshita S, Trop L, Hussey D, Singh K, et al. In-vivo imaging of Alzheimer disease beta-amyloid with [11C]SB-13 PET. Am J Geriatr Psychiatry 2004; 12: 584–95.